Title

Nanoscale Morphology of Doctor Bladed versus Spin-Coated Organic Photovoltaic Films

Journal

Advanced Energy Materials, 7(22)

ISSN

1614-6832

Authors

Pokuri, Balaji Sesha Sarath
Sit, Joseph
Wodo, Olga
et al.

Publication Date

2017-11-01

DOI

10.1002/aenm.201701269

Peer reviewed

Nanoscale Morphology of Doctor Bladed versus Spin-Coated Organic Photovoltaic Films

Balaji Sesha Sarath Pokuri, Joseph Sit, Olga Wodo, Derya Baran, Tayebeh Ameri, Christoph J. Brabec, Adam J. Moule, and Baskar Ganapathysubramanian**

Recent advances in efficiency of organic photovoltaics are driven by judicious selection of processing conditions that result in a "desired" morphology. An important theme of morphology research is quantifying the effect of processing conditions on morphology and relating it to device efficiency. State-of-the-art morphology quantification methods provide film-averaged or 2D-projected features that only indirectly correlate with performance, making causal reasoning nontrivial. Accessing the 3D distribution of material, however, provides a means of directly mapping processing to performance. In this paper, two recently developed techniques are integrated—reconstruction of 3D morphology and subsequent conversion into intuitive morphology descriptors —to comprehensively image and quantify morphology. These techniques are applied on films generated by doctor blading and spin coating, additionally investigating the effect of thermal annealing. It is found that morphology of all samples exhibits very high connectivity to electrodes. Not surprisingly, thermal annealing consistently increases the average domain size in the samples, aiding exciton generation. Furthermore, annealing also improves the balance of interfaces, enhancing exciton dissociation. A comparison of morphology descriptors impacting each stage of photophysics (exciton generation, dissociation, and charge transport) reveals that spin-annealed sample exhibits superior morphology-based performance indicators. This suggests substantial room for improvement of blade-based methods (process optimization) for morphology tuning to enhance performance of large area devices.

1. Introduction

Research into photovoltaic (PV) devices composed of organic materials (organic PV or OPV) have been a recent hot topic because organic materials can be deposited from solution over large areas, which promised to greatly reduce the cost of PV device fabrication.[1,2] In addition, to reduced fabrication cost, OPV layers can be coated onto substrates with nontraditional form factors for building integrated applications.[3–5] Potential advances in flexible transparent substrates also open the possibility of extremely light weight or flexible devices.[6–9] Recent validated device efficiency records of over 10% demonstrate that OPV devices can be fabricated with high power conversion efficiency.[10–15] Also, OPVs have recently been demonstrated to be more efficient than crystalline Si under indoor lighting, opening a niche application for OPV that will require consistent manufacturing.[16] However, it has also been demonstrated that group-to-group consistency is low for the solution-fabricated devices in large part, because small differences in fabrication technique can lead to large differences in device performance.[17] These differences come about because OPV active layers are mixtures of donor polymers with small-molecule acceptors that self-assemble and phase separate during the film-drying process. As a result, the length scale for phase separation and the purity of the domains are a complex product of the donor/acceptor miscibility, solubilities of the donor and acceptor, surface energies of the donor, acceptor, and substrate, drying rate, and postdrying thermal treatments.[18,19]

B. S. S. Pokuri, Dr. B. Ganapathysubramanian
Department of Mechanical Engineering
Iowa State University
Ames, IA 50010, USA
E-mail: baskarg@iastate.edu

J. Sit, Prof. A. J. Moule
Department of Chemical Engineering
University of California Davis
CA 95616, USA
E-mail: amoule@ucdavis.edu

Dr. O. Wodo
Department of Mechanical and Aerospace Engineering
University at Buffalo
State University of New York
Buffalo, New York 14260, USA

Dr. D. Baran, Dr. T. Ameri, Prof. C. J. Brabec
Department of Materials Science and Engineering
Friedrich-Alexander University
i- Meet
Erlangen 91058, Germany

Dr. D. Baran
Materials Science and Engineering
King Abdullah University of Science and Technology
Thuwal 23955, Saudi Arabia

The ORCID identification number(s) for the author(s) of this article can be found under https://doi.org/10.1002/aenm.201701269.

DOI: 10.1002/aenm.201701269

Despite the challenge of controlling self-assembly, the greatest advantage of OPV technology is the ability to coat PV layers quickly and cheaply over large areas. Most efficiency records are made on small-area devices produced using spin coating, which is a solution-coating technique that is difficult to scaleup to large areas.[9,20–22] Recently, there has been significant interest in fabrication of OPV devices using large-area compatible coating methods such as spray coating,[4,5,23–25] slot coating,[22,26] and blade coating.[27–33] Blade coating, in particular, is attractive for rapid exploration because a blade coater is small enough to fit onto a typical fume hood research bench, is compatible with roll-to-roll coating, and makes efficient use of expensive polymer samples. Blade coating has been used to fabricate OPV devices with over 6% efficiency[29,32] and optimized using solvent mixtures for various polymers.[27–32] The optimization of solvent mixtures is used to improve the device efficiency and mutual solubility of polymer (P) and fullerene (F).[32] The optimization of the self-assembly process translates to optimizing the morphology of the donor/acceptor phases. A key step in this process is a comprehensive nanoscale analysis of morphology of the fabricated device and its link to the coating process. A characterization methodology is needed that can accurately characterize the 3D position, orientation, and concentration of materials with nanometer resolution providing more insights into these effects. Even if these data can be acquired, it is necessary to accurately quantify the morphology with descriptors that serve as a basis for quantitative process–structure–property relationship.

While there have been substantial advances in the characterization of OPV films,[34–36] organic donor–acceptor mixture films present huge characterization challenges because they are often amorphous or semicrystalline, limiting the amount of information that can be gleaned from diffraction techniques. Methods like Grazing Incident Wide- and Small-Angle X-ray Scattering (GIWAXS and GISAXS) give information about the orientations of polymer crystals in the film but are unable to provide information about amorphous domains or to quantify the absolute amount of phase separation or crystallinity in the film. Ultrafast spectroscopic techniques can provide information about the average domain size and average lifetimes of excited states, but they are unable to provide real space information because the phase separation is on a much smaller length scale than the visible or UV wavelengths. OPV films are mostly composed of light elements (C, H, S, O, N, and F), which provide low scattering contrast for both X-rays and electron beams. For this reason, electron microscopy provides little bright field or dark field contrast for organic mixtures. Further, most transmission electron microscopy methods (TEM) give a 2D projection of the 3D object, which averages composition information vertically through the sample.[37] In order to obtain 3D information, it is usually necessary to perform electron tomography (ET), in which a series of images are taken at different angles between the sample and the film followed by numerical reconstruction into a 3D volume. Initial ET images of OPV films used the scattering contrast between crystalline and amorphous domains to create images. It was possible to distinguish between crystalline and noncrystalline domains, but the domain composition could not be quantified. However, amorphous domains with differing compositions are not distinguishable.[38–41] Recent work on energy-filtered TEM makes use of spectroscopic and real space information simultaneously. High energy losses by core electrons of specific elements (C or S)[42] or low energy losses by the surface phonons of the molecules[43] are used to create contrast between donors and acceptors. In some cases, this information was converted to tomographic images that could give spatial, but not concentration information in three dimensions.[44] In a recent work, we used an acceptor molecule Lu@C_{80}-PCBEH with heavy metals to create scattering contrast between donor and acceptor phases.[45,46] In this case, the contrast is very high because each acceptor molecule has three Lu atoms in it.[47,48] Additionally, this fullerene has very similar mixing properties and current-voltage (I-V) characteristics to $PC_{60}BM$ and $PC_{70}BM$ that are the most common acceptors used in OPV research.[45] To further refine the image reconstruction we used the discrete area reconstruction technique (DART), which improves the assignment of domain interfaces, reduces errors from missing wedge artifacts, and allows the assignment of relative gray levels in mixed samples.[49,50] We used the combination of increased contrast, DART, and quantitative mass balance between phases to reconstruct P3HT/Lu@C_{80}-PCBEH tomographic images with pure P3HT, mixed P3HT/Lu@C_{80}-PCBEH, and Lu@C_{80}-PCBEH-rich phases. In addition, we were able to quantify these data for analysis of charge transport properties[51] and vertical phase segregation.[52] Comparison against vertical concentration measurements from reflectometry shows qualitative agreement in all concentration features, but missing vertical concentration information due to the missing wedge artifact.[52]

In this paper, we build upon the imaging and characterization strategies that we previously reported to analyze OPV morphologies obtained from blade- and spin-coating P3HT/Lu@C_{80}-PCBEH mixtures both before and after thermal annealing. We use scanning transition electron tomography (STET) to reconstruct and compare morphologies with 3D nanoscale resolution. Morphology reconstructions show a mixture of pure P3HT, acceptor-rich and mixed phase (M) regions. We take the further step of quantifying how the differences in morphology affect exciton quenching and charge transport to the electrodes in these films. We use graph-based analysis techniques to convert the reconstructed morphology into intuitive descriptors that represent various performance indicators (exciton generation, dissociation, and charge transport). For example, to estimate exciton dissociation characteristics, we analyze the mean/effective distance that a generated exciton must diffuse to be quenched at the nearest donor/acceptor interface. To predict charge transport characteristics, we look at volume fractions of each phase connected to the electrodes. We find that an annealed spin-coated sample imparts a near-perfect balance of paths to respective electrodes and thus an optimized morphology for OPV applications. In contrast, both annealed and unannealed doctor-bladed samples had better donor connectivity than acceptor connectivity and thus would be expected to demonstrate poorer OPV efficiency. These analyses give deeper insights into the morphological effect of processing conditions on the performance of a device. More importantly, by analyzing morphologies before and after thermal annealing, we show how various stages in the fabrication process can help/hinder certain aspects of performance. Because we analyze true 3D morphologies, we envision that these procedures can link the coating process to the resultant morphology and device performance.

2. Results

A series of thin films fabricated with four fabrication conditions were measured using STET and the reconstructed volumes were quantified. **Figure 1** shows the morphologies from all four fabrication methods, along with the volume fraction of each phase. The spatial distribution of the acceptor (A) (purple), donor (D) (blue), and mixed (M) regions (green) is displayed to provide a visual indication of the spread and distribution of the three phases (see Videos S1–S4 in the Supporting Information for an immersive walk-through of the donor phase distribution in the films). Three trends are clearly noticeable. The first is that relaxation by thermal annealing results in "precipitation" of the donor from the mixed phase to form more of the pure-donor phase. Correspondingly, there is a decrease in the volume fraction of the pure acceptor phase. The second trend is that annealing only minimally changes the volume fraction of the mixed phase for both blade-coated and the spin-coated samples. Finally, spin coating yields a larger volume fraction of pure P3HT phases than blade coating.

Spin coating followed by annealing seems to result in a balanced volume fraction (≈19%) of pure donor and pure acceptor phases. This is indicative of superior charge dissociation and transport behavior, as subsequent analysis later in the paper reveals. To further explore the effect of processing (especially surface and shear effects), we look at the vertical distribution of the material in the films in **Figure 2**. Interestingly, we show that the as-cast blade-coated sample exhibits a significantly higher degree of uniformity in the vertical distribution of all three phases than the as-cast spin-coated sample. Comparing the coating methods, spin coating is expected to induce a higher shear than blade coating. In addition, the spin-coated film dries with a relatively higher reduction in surface temperature on a room temperature substrate compared to a blade-coated film that dries on a substrate heated to 70 °C. Also, the spin-coated sample has a skin layer of P3HT at both interfaces as was reported previously,[53,54] while the blade-coated sample does not appear to have this skin layer. It is difficult to quantify the composition at the interfaces using STET because surface roughness affects the density distribution at the interfaces and artificially increases the apparent polymer prevalence. We correct for this by removing surface data that appear to be an artifact, but at the same time lose information about real surface composition.

Thermal annealing greatly increases the density of the donor phase in both samples as previously reported.[55,56] However, the impact on vertical composition distribution is dramatically different. While annealing results in nearly equal

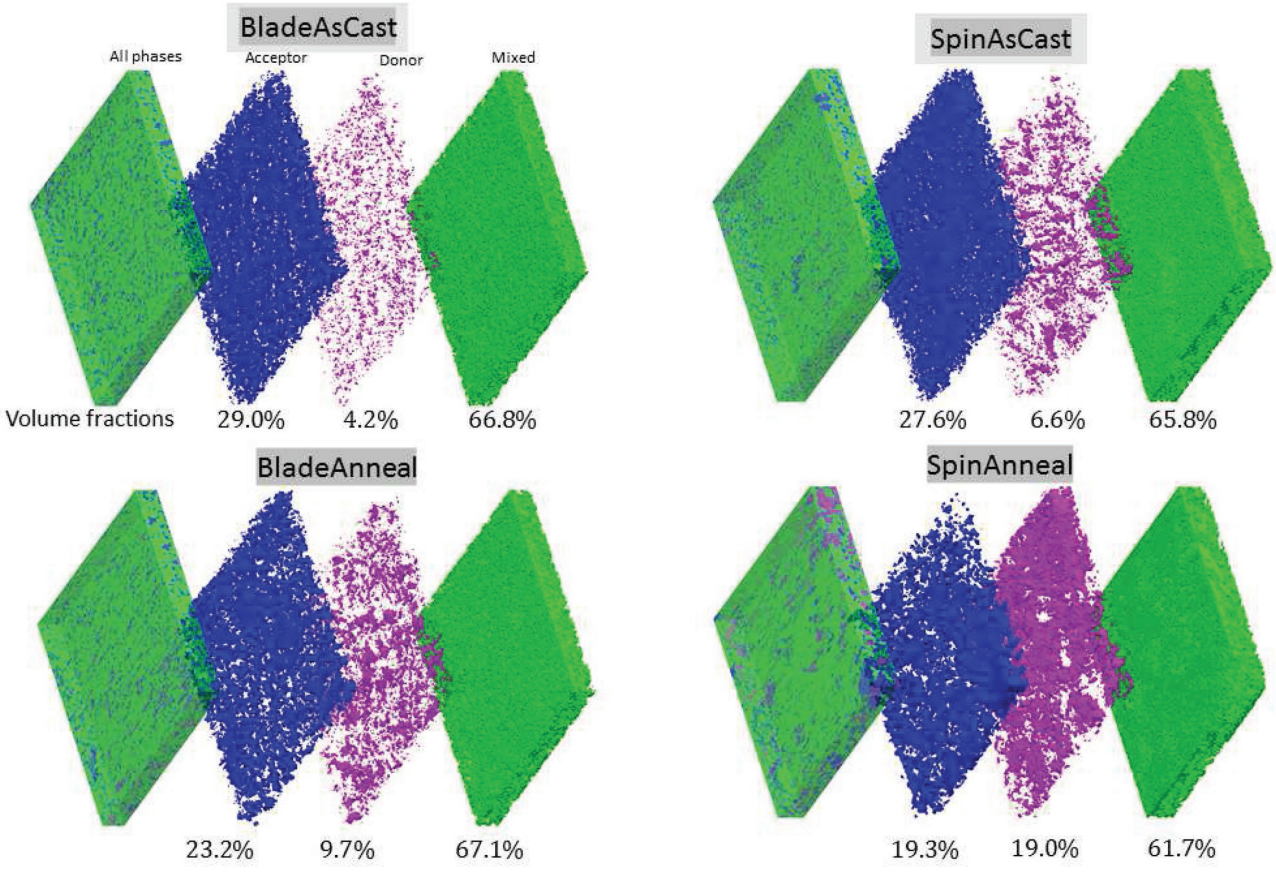

Figure 1. Reconstructed morphologies and isovolumes of acceptor, donor and mixed for the four different samples (BladeAsCast, BladeAnneal, SpinAsCast, and SpinAnneal). Below each iso-volume representation, the volume fraction of the phase is provided.

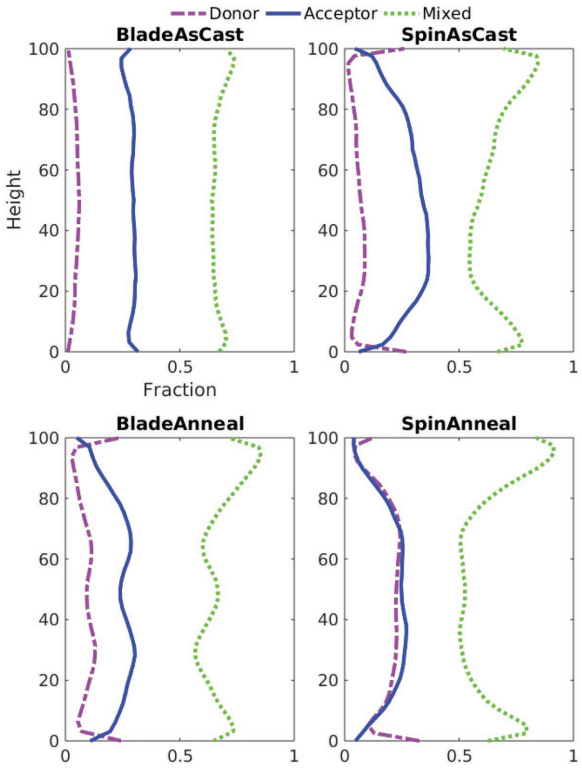

Figure 2. Vertical distribution of donor, acceptor, and mixed phases.

vertical distribution of pure donor and pure acceptor phases in the spin-cast sample, the blade-cast and annealed samples have uniformly less pure donor phase. Previous measurements of vertical distribution of spin-cast and annealed P3HT/Lu@C80-PCBEH samples showed a flat distribution of pure acceptor phase and a concentration of pure donor phase near the center of the film as seen here. We posit that the differences in the vertical distribution of materials seen previously and here are due to the higher M_W of the P3HT. Also the previous samples were spin-cast from chlorobenzene and heated to 150 °C, while here the samples were cast from dichlorobenzene (DCB) and then annealed at 140 °C.[48,51,52] For both annealed samples, there is a much higher content of mixed phase near both interfaces, which is consistent with all previous tomography measurements.[48,51,52]

Figure 3 shows the relative interfacial area between individual phases, D–M, D–A, and A–M. Regardless of the processing, all films show nearly zero amount of donor–acceptor interface as previously reported.[51] This lack of D–A interface confirms that the mixed phase is distributed between the donor and acceptor phases. Annealing enhances the amount of D–M interface content with the increase of donor phase volume fraction. The A–M interface area decreases for both spin-cast and blade-cast samples, also proportional to the reduction in acceptor volume fraction. This further strengthens the observation that annealing essentially moves the acceptor from a pure phase to a mixed phase, while "precipitating" out the donor from the mixed phase to a pure donor phase. This observation is not consistent with the previous measurement of spin-cast films using chlorobenzene as the casting solvent. In that case, almost all of the volume was kinetically trapped in the mixed phase, and both the donor and acceptor phases increased in volume fraction upon thermal annealing.[48] It can also be seen that the spin-cast and annealed sample has a very balanced distribution of D–M and A–M interface fractions. The balanced ratio of D–M and A–M interface areas is consistent with our previous work.[51] Finally, the differences in the volume fractions and surface areas of the samples seen here and in previous measurements show that our understanding of the combined effects of polymer M_W, polydispersity, regioregularity, weight ratio of the donor and acceptor, solvent quality, drying time, annealing temperature, and coating-induced shear is still not sufficient, in spite of thousands of papers of exhaustive research on P3HT/fullerene mixtures, to provide predictive information about morphology development.

2.1. Exciton Dissociation Measures

Having looked at coarse scale measures, we next focus on extracting descriptors that correlate with the exciton dissociation capacity of these morphologies. We quantify this by calculating the path lengths of all potential locations of exciton generation in pure phases to the nearest interface of the mixed phase (where charge separation occurs). We assume that excitons

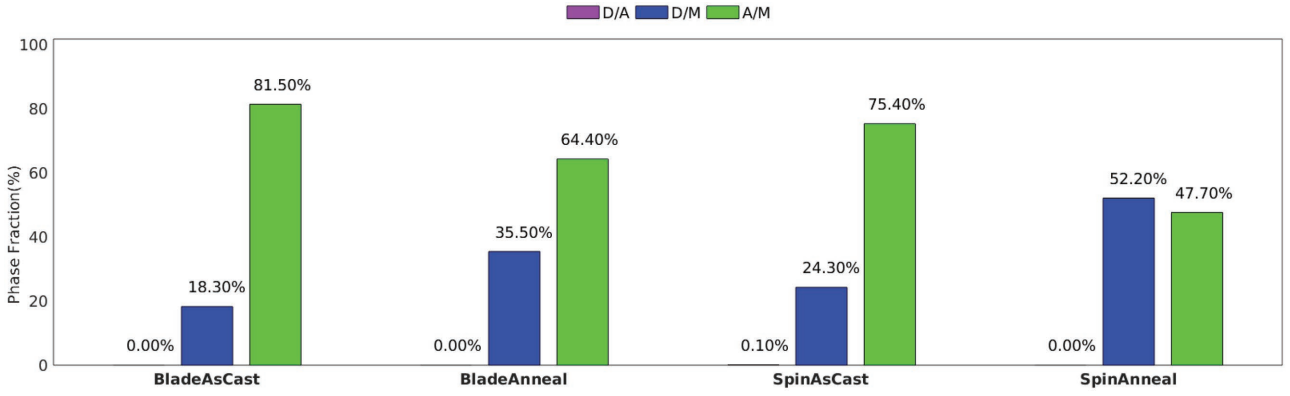

Figure 3. The distribution of interfaces between D/A, D/M, and A/M across the four samples. The complete lack of D/A interface indicates that the mixed phase lies in between the pure donor and pure acceptor phases.

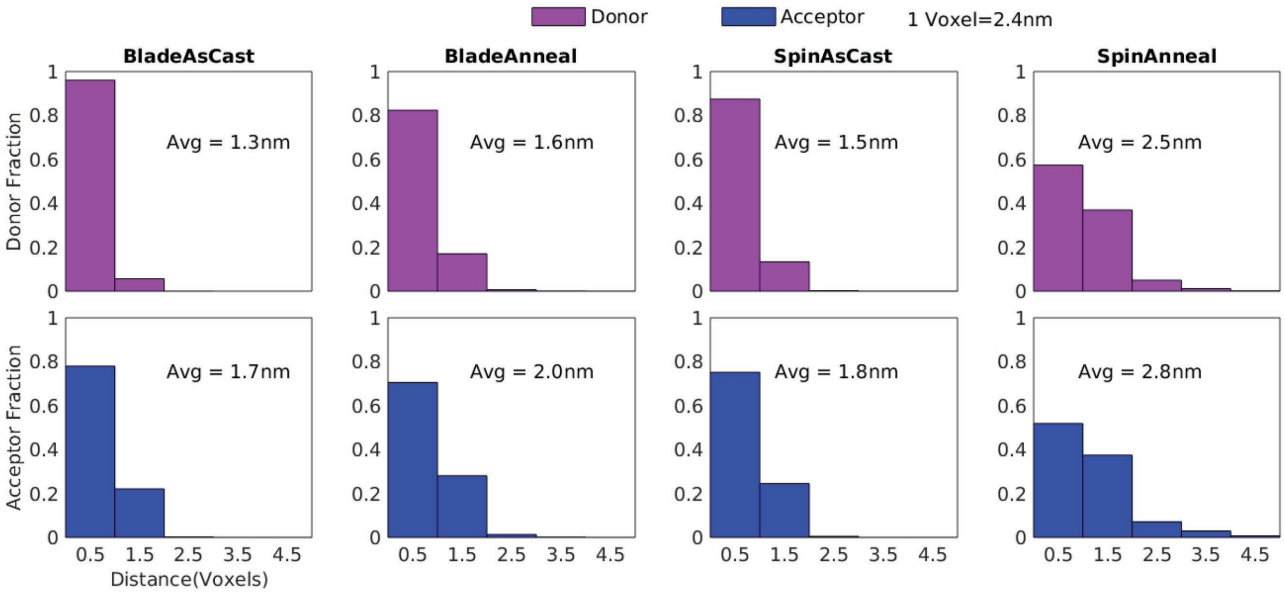

Figure 4. Exciton dissociation measure. The distance distribution of donor (top row) and acceptor (bottom row) voxels to the nearest interface (D/M or A/M) is shown as a histogram.

generated within a mixed phase have a 100% probability of dissociating. Within pure phases, excitons generated at locations closer to an interface have a higher probability of successfully dissociating to create viable charge carriers. While fluorescence-quenching measurements can be used to estimate exciton dissociation efficiency in terms of an average spherical domain size,[57] our graph-based approach allows direct calculation of the path length (distance) to the nearest interface for "every" voxel in the morphology. Based on all path lengths, histograms (**Figure 4**) are constructed, which also report the average distance to the interface (which would be indicative of the domain size radius assuming a spherical domain). We see that the distribution of distances to the mixed phase interface for acceptor-rich and donor-rich phases is very similar, independent of the processing history. As expected, thermal annealing broadens the distribution of the distances to the interfaces, indicating an increase in the average domain size. This is also clearly seen in Figure 1. Most importantly, the average distance to the dissociating interface for all four cases is much smaller than the average exciton dissociation length (≈7 nm).[57,58] This suggests that all four samples suffer minimal geminate recombination and will exhibit high internal quantum efficiency.

2.2. Charge Transport Measures

We next construct descriptors that quantify various aspects of charge transport capabilities of the four samples. As a first measure, we identify the connectivity of the domains with the respective electrodes. This descriptor is computed by identifying the number of donor voxels connected directly (meaning without going through another phase) to the anode or acceptor voxels directly connected to the cathode or mixed phase voxels connected to either electrode (**Figure 5**). Note that pathways against electric field are treated the same as those in the direction of electric field. We efficiently perform this calculation using connected components algorithm for graphs. It can be observed that the acceptor and mixed phases exhibit a very high connectivity to the electrodes, regardless of the processing

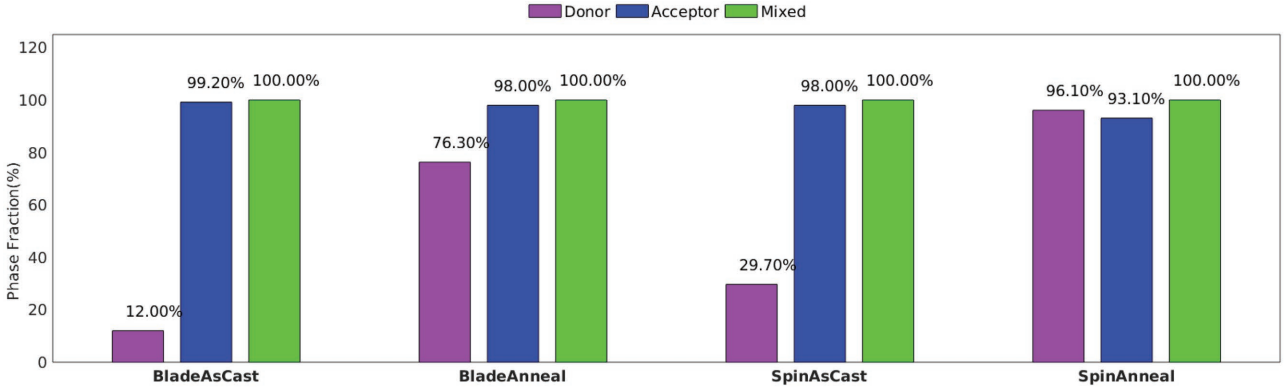

Figure 5. Charge transport measure: the connectivity of each phase to the respective electrode.

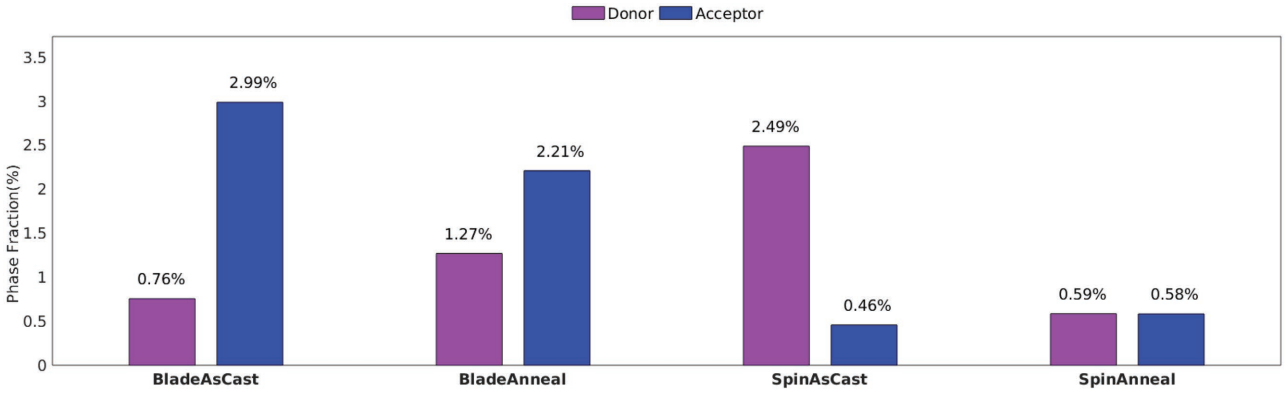

Figure 6. Charge transport measure: the fraction of total volume with "straight rising" paths to the corresponding electrode.

conditions, which are consistent with previous STET measurements.[51] The as-cast samples show low connectivity of the donor phase to the anode, which can be attributed to the low volume fraction (Figure 1) of donor-rich phase in these samples and can be correlated to poor hole mobility in as-cast P3HT/PCBM films.[59,60] Annealing increases the volume fraction of donor-rich phase; the connectivity is also increased substantially.[61] Here, it is also clear that spin-cast samples have higher donor-phase connectivity both before and after annealing, which should indicate better transport of holes to the anode compared to blade-cast samples. This result shows that significant research is needed to optimize the blade-coating conditions, in particular substrate temperature and solvent to affect drying rate, which, in turn, can be used to optimize the formation of donor phases.[62] We see that purely relying on postannealing is not sufficient to improve charge transport pathways.

While high connectivity is necessary for good charge transport, high connectivity alone may not be sufficient to guarantee good charge transport characteristics. This is because connectivity does not consider the actual transport path length that charges must take to reach the electrodes. Morphologies exhibiting longer charge transport pathways could suffer higher rates of recombination. We therefore next quantify the charge transport path lengths across the four samples. First, we measure the charge transport length from each voxel in a pure phase to the respective electrode. Next, we identify the fraction of the volume of each phase that is connected to an electrode and exhibits "perfect" charge transport pathways. By perfect, we mean the shortest possible charge transport pathway from a voxel to the respective electrode. We call this pathway a "straight rising" pathway, since the shortest path is simply the straight line from that voxel to the electrode. **Figure 6** shows this fraction of "straight rising" paths (of the total volume) to the respective electrodes. Figure 6 (in conjunction with the morphology shown in Figure 1) suggests that only a very small fraction of the volume (irrespective of the processing) has low tortuosity (or is a straight rising path).

As a final measure of charge transport, we consider the relative distances that complementary charges must travel to be collected, which is a more detailed and perhaps important measure than the comparison of hole and electron mobilities that is standard.[59,63] We consider a morphology to have a well-balanced structure if there is a good overlap between the distribution of hole-transport pathways and electron-transport pathways. We compute this in the following way: for each voxel in the morphology the (shortest) distance (along the respective phase) to the corresponding electrode is computed using a graph shorted path algorithm (Dijkstra's algorithm). Using this charge transport distance, we compute the tortuosity of the path that a charge (starting from a voxel) must endure to get to its electrode. The tortuosity is the ratio of the actual distance to the shortest linear distance to the electrode (the tortuosity distribution for each of the acceptor-/donor-rich phases is provided in the Supporting Information (Figure A2). Using the tortuosity distribution allows us to identify what fraction of the donor and acceptor phases exhibit similar tortuosity. This provides a measure of balance in pathways. A balanced tortuosity distribution suggests that for every donor voxel with a very tortuous pathway for a hole to reach the electrode, there is a complementary acceptor voxel that exhibits a similarly tortuous pathway for an electron to reach its electrode. **Figure 7** shows this plot. It can be inferred from the plots that as-cast samples show very little balance in charge transport pathways. Both blade- and spin-cast samples show large variation in the fraction of "isotortuous paths" comparing the acceptor- and donor- rich phases. Thermal annealing significantly improves the balance of pathways for both coating methods. However, it is clear that spin coating plus annealing yields balanced charge pathways for holes and electrons, while blade coating plus annealing yields a higher tortuosity for holes in donor phases than for electrons in acceptor phases. This mismatch can be seen to originate in the lower volume fraction of pure donor phase and the reduced charge pathways for holes, which is shown in Figure 5.

All of these results taken together show that if OPV devices are to be mass produced using a roll-to-roll coating method; significant research is needed to optimize the coating conditions that yield better charge transport characteristics. This result could be achieved by changing one of several blade-coating fabrication parameters: for example, by increasing the ratio of P3HT to fullerene in the coating solvent,[64] by reducing the substrate temperature to allow longer drying times and thus more P3HT crystallization,[60,62] by addition of a solvent additive to induce phase segregation in P3HT/fullerene,[65,66] or by changing the casting solvent to affect better phase segregation the P3HT/fullerene.[67,68]

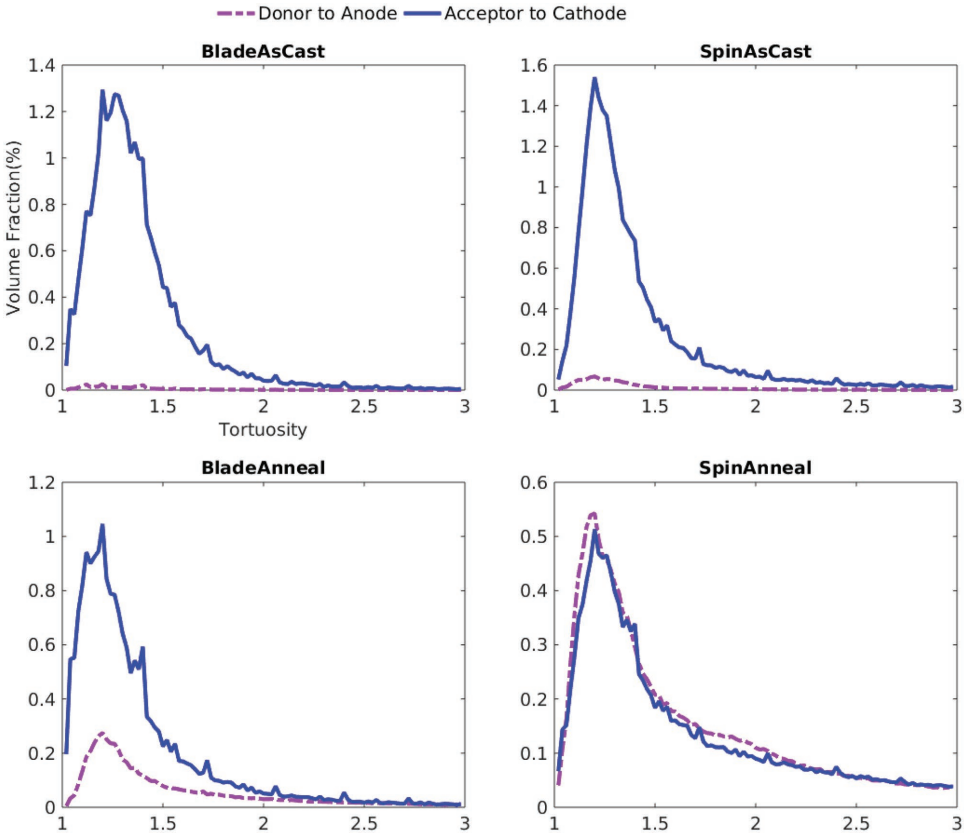

Figure 7. Charge transport measure: the path length (in terms of the tortuosity) distribution of all voxels to their corresponding electrode. This provides a measure of balance of pathways, essentially illustrating the difference in charge transport pathways for electrons versus holes. Note that this does not include the fraction with "straight rising" paths that are shown in Figure 6.

3. Conclusions

In this paper, we used scanning transmission electron tomography and discrete area reconstruction technique to generate quantitative 3D nanoscale position and concentration specific maps of P3HT/Lu@C80-PCBEH bulk-heterojunction organic photovoltaic devices. We specifically studied how the use of spin coating versus blade coating affected the resulting morphology in as-cast and thermally annealed films. All the imaged films could be described using a three-phase morphology consisting of pure donor (crystalline-P3HT), acceptor-rich (amorphous Lu@C80-PCBEH), and a mixed phase of amorphous P3HT mixed with Lu@C80-PCBEH. The mixed phase is distributed directly between pure donor and acceptor phases. It can be inferred that excitons formed in pure phases of either polymer or fullerene will undergo charge separation at the interphase between a pure and a mixed phase. In all films measured in this study, the distance between a pure phase voxel and a mixed phase voxel, which corresponds to the distance that an exciton must diffuse before charge separating at a donor/acceptor interface, is far smaller than the typical exciton diffusion length. This strongly suggests that the exciton separation step is expected to occur with ≈100% efficiency in all measured morphologies.

Comparing spin-coated and blade-coated films, we found that spin-coated films had a larger volume fraction of pure P3HT phases both before and after thermal annealing the films. Referring to the vast literature on P3HT/fullerene processing, it appears that control of the drying time and/or control of the P3HT aggregation using solvent additives could be used to increase the volume fraction of the P3HT phase in the as-cast film. This study shows that thermal annealing is not sufficient to increase the pure P3HT volume fraction in the blade-cast film to match the pure P3HT volume fraction in the spin-coated film. The consequences of reduced P3HT volume fraction in the blade-coated film are reduced charge transport pathways (volume fraction) to the anode. The reduction in charge pathways results in a more tortuous pathway for holes to reach the anode compared to electrons, which is summarized as an unbalanced, tortuous pathway. Spin-coating plus annealing yields a balanced charge pathway and, as seen in many articles, a high internal quantum efficiency and fill factor in OPV devices. Thus, we can conclude that more research is needed to determine the fabrication conditions in blade-coated films that will yield optimized device characteristics, with particular focus on enhance charge transport.

4. Experimental Section

Figure 8 shows the various stages of the analysis pipeline. Each stage of the pipeline was discussed below.

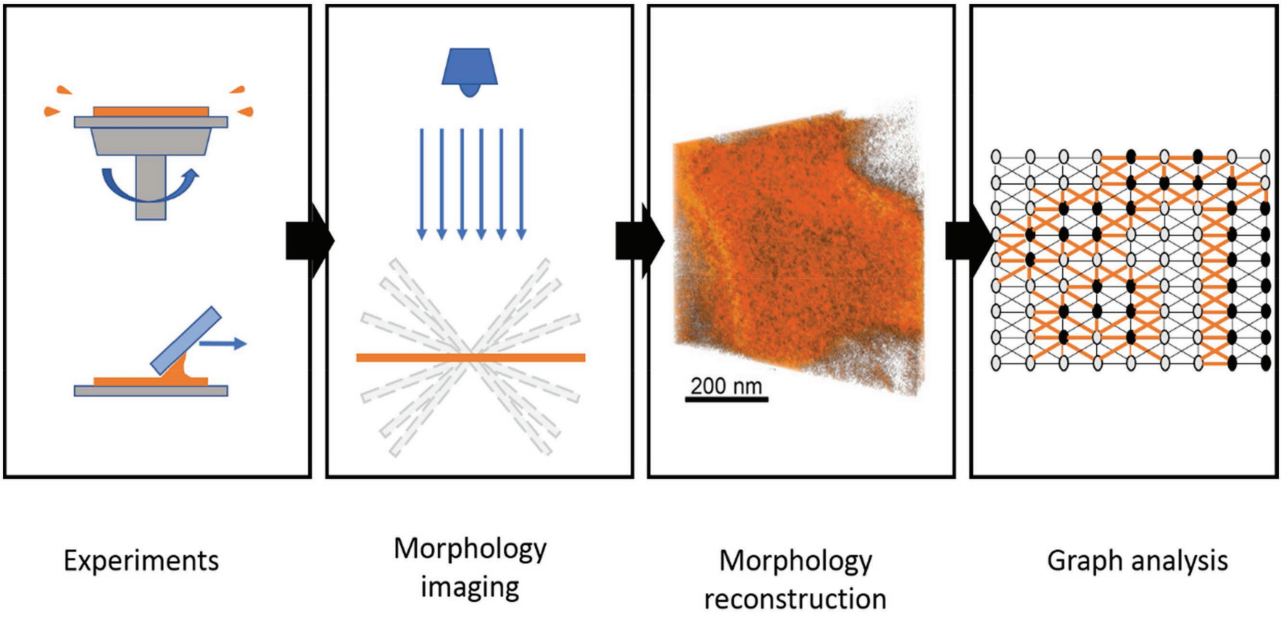

Figure 8. Workflow of the experiment–imaging–analysis pipeline. The experiment consists of fabricating thin films using two sets of fabrication processes (spin coating and doctor blading). HAADF-STEM imaging is performed on the thin films, and the morphology is reconstructed with the DART algorithm. Noise removal and feature extraction are finally performed using graph-based analysis.

Materials and Fabrication Protocol: The materials used were purchased from Merck (P3HT) and Luna Nanoworks (Lu@C80-PCBEH). All samples were coated onto glass substrates that were coated with Poly(3,4-EthyleneDioxyThiophene) PolyStyrene Sulfonate (PEDOT:PSS) from (Clevios P). P3HT/Lu@C80-PCBEH blends were prepared using spin-casting and blade-coating techniques from *o*-DCB solutions with 20 mg mL^{-1} total concentration. The 1:1 (w:w) P3HT:PCBM (phenyl-C_{61}-butyric acid methyl ester) and 1:1.3 (w:w) P3HT/Lu@C80-PCBEH (Phenyl-C61 Butyric acid 2-ethylhexyl ester) solutions from *o*-DCB were prepared and kept at 70 °C overnight for better mixing. The spin-casting method was used to obtain 100 ± 5 nm films. Thermally annealed films were annealed at 140 °C for 10 min in an inert atmosphere to enable P3HT crystallization and phase separation. Solutions were blade-coated using 15 mm s^{-1} blade speed at 70 °C to yield 100 ± 5 nm films after drying. The same annealing conditions were applied to blade-coated films in an inert atmosphere.

Morphology Imaging—HAADF-STEM Protocol: For STET imaging, samples were floated onto the surface of a water bath by dissolving the water soluble PEDOT:PSS layer in deionized water. Then flakes of the bulk-heterojunction layer were picked up onto lacey carbon TEM 200 mesh grid. Imaging for electron tomography reconstructions was conducted using high angle annular dark field scanning transmission electron microscopy (HAADF-STEM) using a JEOL 2100F transmission electron microscope (JEOL Ltd, Tokyo, Japan) operated at 200 kV. The tilt series was taken using dynamic focus via a STEM tomography plugin for Digital Micrograph (Gatan). Images were acquired at 1° intervals from at least +65° to −65°.

Morphology Reconstruction—DART Algorithm: HAADF-STEM images were manually aligned using IMOD.[69] Volume reconstructions were then performed in MATLAB using a custom code to implement DART by using HAADF-STEM images as an input. Gray levels and thresholds were adjusted in DART until the difference between the reconstruction volume and original microscopy images (back projection error) was minimized. Full details on the reconstruction methods are published elsewhere.[70,71] The reconstruction process usually results in the inclusion of surface layers of noise which have to be removed.[52] Previously, surface layers were removed by visual inspection of the reconstructed morphology, which resulted in an admittedly subjective removal of surface layers. In this work, concepts from computational homology were utilized to characterize the morphology in a layer-by-layer fashion. Surface layers that are not part of the thin film are noisy with no long-range structure, thus exhibiting a large number of small components of connected voxels of each phase. This is quantified in computational homology in terms of the zeroth Betti number (β_0). Thus, a layer-by-layer plot of the zeroth Betti number shows a jump when a surface noise layer is encountered (**Figure A1**), which results in an objective criterion to identify and remove surface layers.

Morphology Analysis—GraSPI: The 3D morphologies resulting from the reconstruction were converted into an equivalent graph. It was previously shown that representing morphologies as graphs enables using very efficient and sophisticated algorithms to computationally characterize and interrogate complex morphologies.[51,72,73] Since each stage of the photophysics intimately depends on the 3D morphology, graph-based algorithms were used to compute metrics that served as meaningful performance descriptors of each stage. This includes morphology descriptors that quantify light absorption, exciton diffusion, exciton dissociation, and charge transport.[74] This was shown to be an especially useful tool when looking at tomography data that exhibit complex 3D morphological variations and are of large size. In particular, the morphology was characterized in terms of the size, shape, and topology of donor-rich domains as a measure of light absorption and exciton dissociation, the proportion of acceptor–mixed (A–M)/mixed–donor (M–D)/acceptor–donor (A–D) interfaces as a measure of exciton dissociation, and types of paths to electrodes as an indicator of charge transport.

Appendix

A.1. Preprocessing

Utilizing the above-mentioned imaging technique, surface roughness in the film may be interpreted as a polymer rich region, precluding information about film boundary. This misrepresentation becomes a significant challenge, as it affects estimation of charge transport traits of the film. In the current work, we use principles from computational homology to identify and isolate layers of morphology that are potentially due to imaging artifact. For example, air (on a rough surface) is usually imaged as noisy data. Noisy data have a very small correlation length and form more isolated clusters, often 1 voxel in thickness, in contrast to the film which consists of much larger clusters. The number of

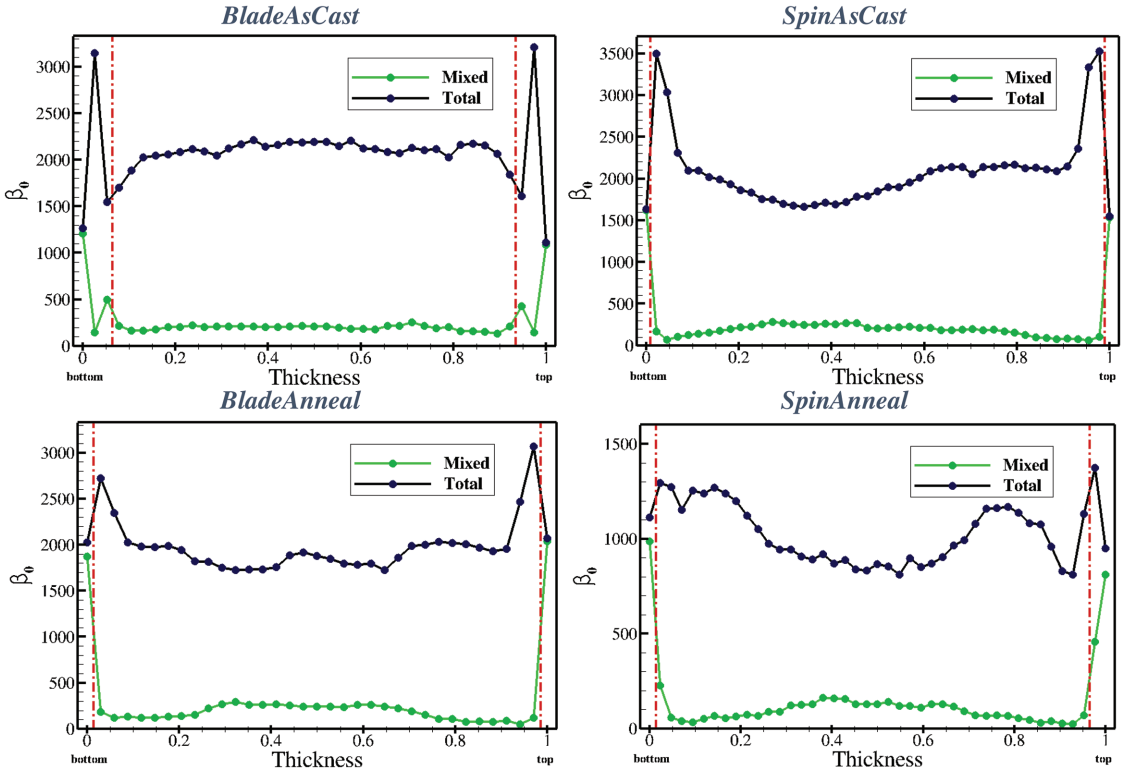

Figure A1. Plot of Betti numbers for each sample. The red lines indicate the new boundary of the film after preprocessing. Layers with high total β_0 were discarded to account for any imaging artifact.

clusters per layer is represented in computational homology as zeroth Betti number (β_0). In graph theory, the zeroth Betti number (β_0) is given by the number of connected components. For each voxel layer of morphology, we compute the number of connected components in the sample. Figure A1 shows the sum of connected components of each of the three phases per layer. We can observe that two of the top and bottom layers have a large β_0 compared to all other layers. However, this can be deceptive as noise in one phase can dominate the sum of β_0 per layer. Therefore, we look at the β_0 of the largest phase in the film of the mixed phase. This can give better information for deciding the number of voxel layers to be removed for proper analysis of morphologies. Following figure plots the β_0 of the mixed phase, per layer, we remove the following number of layers: (a) *BladeAsCast*: 3-top, 3-bottom; (b) *BladeAnneal*: 1-top, 1-bottom; (c) *SpinAsCast*: 1-top, 1-bottom; (d) *SpinAnneal*: 2-top, 1-bottom.

A.2. Mass Analysis

In this section, we show that cropping the morphologies using principles from computational homology does not alter the relative mass contents of the polymer and fullerene. Classification of a "voxel" as P, F, or M is based on the threshold provided in **Table A1**.

A.3. Tortuosity Distribution

We discuss tortuosity distribution in the films. This supplements the discussion on the straight rising paths in the main text. Tortuosity is calculated for all voxels in the domain which have a path to the respective electrode through voxels of the same phase. (To reiterate, tortuosity of a path is defined to be the ratio $\frac{L_c}{L_s}$; where L_c is the length of the charge transport pathway from a voxel to the electrode; and L_s is the shortest straight path from that voxel to the electrode (same as the length of charge pathway for a straight rising path)). Results for this

Table A1. Composition (mass%) of polymer and fullerene in each phase and volume fraction before and after cropping. Calculating the mass fraction of polymer and fullerene for each sample indicates that the original ≈1:1 ratio is not affected by the removal of the "noisy" layers. Although the change is very small, it nonetheless makes the system very close to the original mass% ratio.

(a) BladeAsCast		
Phase (%D–%A)	Vol% before cropping	Vol% after cropping
Polymer-rich (100–0)	9.8	4.2
Fullerene-rich (42–58)	28.0	29.0
Mixed (59–41)	63.2	66.8
(b) BladeAnneal		
Phase (%D–%A)	Vol% before cropping	Vol% after cropping
Polymer-rich (100–0)	14.3	9.7
Fullerene-rich (29–71)	21.9	23.2
Mixed (58–42)	63.0	67.1
(c) SpinAsCast		
Phase (%D–%A)	Vol% before cropping	Vol% after cropping
Polymer-rich (100–0)	10.6	6.6
Fullerene-rich (32–68)	26.4	27.6
Mixed (62–38)	63.0	65.8
(d) SpinAnneal		
Phase (%D–%A)	Vol% before cropping	Vol% after cropping
Polymer-rich (100–0)	18.1	19.0
Fullerene-rich (3–97)	22.5	19.3
Mixed (58–42)	59.4	61.7

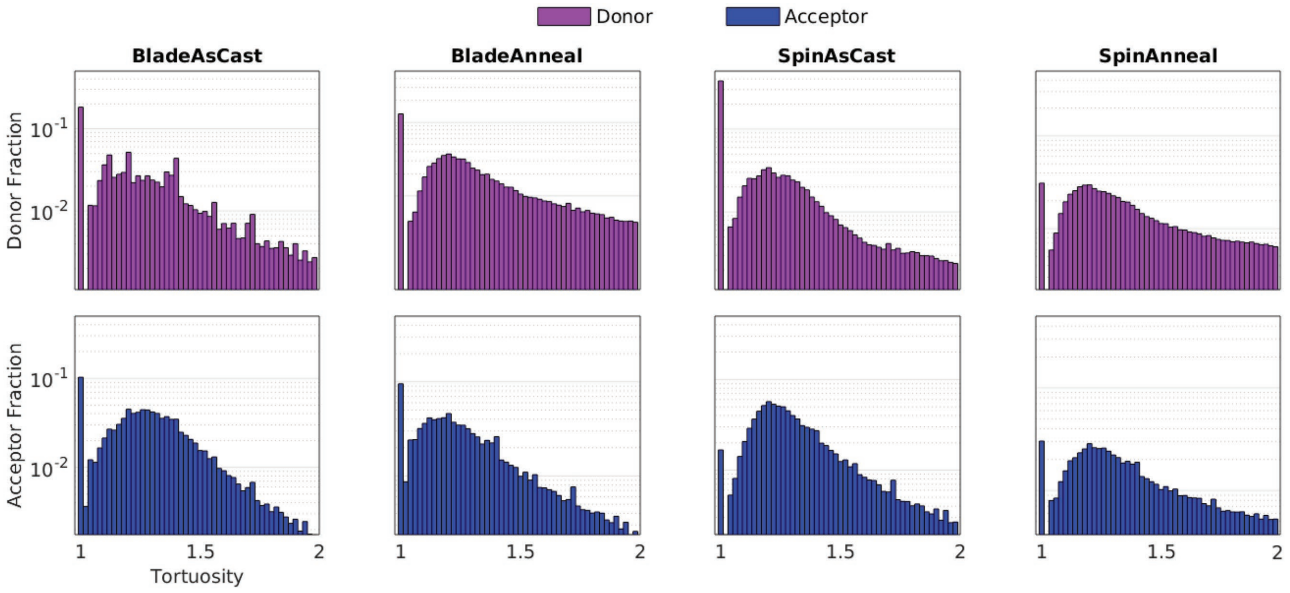

Figure A2. Histogram of tortuosity distribution of pure phases to the respective electrode. Note the log scale of the fractions.

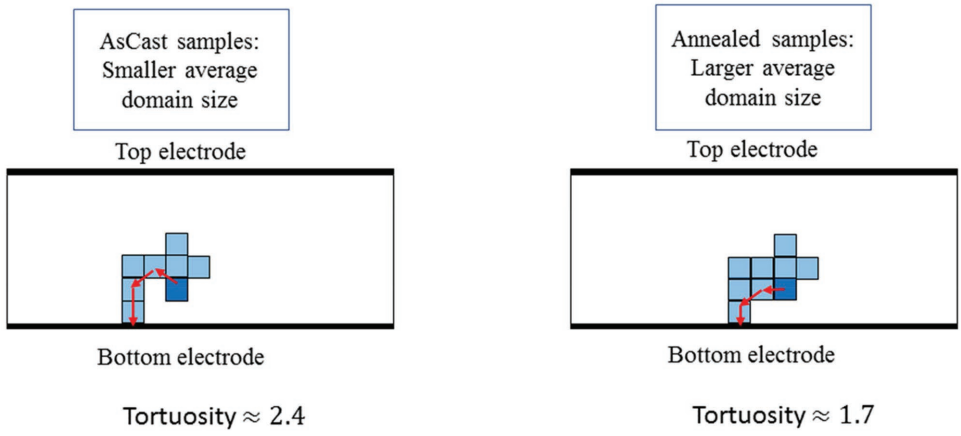

Figure A3. Explanation for smoothening of tortuosity distribution upon annealing (blade-coated sample). We speculate that this is due to an interplay between solvent extraction rate, shear rate, and time of processing the samples.

calculation are shown in **Figure A2** in the form of histograms. The effect of annealing on the average domain size can be seen as widening of the tortuosity distribution. This widening of the distribution is primarily because more pure acceptor (and donor)-rich regions are formed during annealing. We also observe the tortuosity distribution becoming smoother upon annealing. This smoothing is primarily due to improved charge transport pathways (as shown in **Figure A3**) arising from removal of cul-de-sacs during annealing. Interestingly, such doubly curved pathways (as shown in Figure A3) are not prominently observed in the spin-coated samples. We speculate that there is an intricate interplay between solvent extraction rate, coating speed (shear rate), and the durations of coating. This is a rich area for further analysis using full-scale models.[75]

Supporting Information

Supporting Information is available from the Wiley Online Library or from the author.

Conflict of Interest

The authors declare no conflict of interest.

Keywords

blade spin as-cast anneal, internal morphology analysis, organic photovoltaic cells, reconstruction, tortuosity connectivity fraction

Received: May 9, 2017
Revised: June 1, 2017
Published online:

[1] N. Li, P. Kubis, K. Forberich, T. Ameri, F. C. Krebs, C. J. Brabec, *Sol. Energy Mater. Sol. Cells* **2014**, *120*, 701.
[2] N. Espinosa, M. Hösel, M. Jørgensen, F. C. Krebs, *Energy Environ. Sci.* **2014**, *7*, 855.

[3] J. Adams, G. D. Spyropoulos, M. Salvador, N. Li, S. Strohm, L. Lucera, S. Langner, F. Machui, H. Zhang, T. Ameri, M. M. Voigt, F. C. Krebs, C. J. Brabec, *Energy Environ. Sci.* **2015**, *8*, 169.
[4] E. Treossi, A. Liscio, X. L. Feng, V. Palermo, K. Mullen, P. Samori, *Appl. Phys. A: Mater. Sci. Process.* **2009**, *95*, 15.
[5] K. X. Steirer, M. O. Reese, B. L. Rupert, N. Kopidakis, D. C. Olson, R. T. Collins, D. S. Ginley, *Sol. Energy Mater. Sol. Cells* **2009**, *93*, 447.
[6] A. Pierre, M. Sadeghi, M. M. Payne, A. Facchetti, J. E. Anthony, A. C. Arias, *Adv. Mater.* **2014**, *26*, 5722.
[7] L. B. Hu, H. S. Kim, J. Y. Lee, P. Peumans, Y. Cui, *ACS Nano* **2010**, *4*, 2955.
[8] F. C. Krebs, M. Jorgensen, K. Norrman, O. Hagemann, J. Alstrup, T. D. Nielsen, J. Fyenbo, K. Larsen, J. Kristensen, *Sol. Energy Mater. Sol. Cells* **2009**, *93*, 422.
[9] F. C. Krebs, S. A. Gevorgyan, J. Alstrup, *J. Mater. Chem.* **2009**, *19*, 5442.
[10] Y. Liu, J. Zhao, Z. Li, C. Mu, W. Ma, H. Hu, K. Jiang, H. Lin, H. Ade, H. Yan, *Nat. Commun.* **2014**, *5*, 5293.
[11] N. Li, C. J. Brabec, *Energy Environ. Sci.* **2015**, *8*, 2902.
[12] J. You, L. Dou, K. Yoshimura, T. Kato, K. Ohya, T. Moriarty, K. Emery, C.-C. Chen, J. Gao, G. Li, Y. Yang, *Nat. Commun.* **2013**, *4*, 1446.
[13] S. Zhang, L. Ye, J. Hou, *Adv. Energy Mater.* **2016**, *6*, 1502529.
[14] D. Baran, R. S. Ashraf, D. A. Hanifi, M. Abdelsamie, N. Gasparini, J. A. Röhr, S. Holliday, A. Wadsworth, S. Lockett, M. Neophytou, *Nat. Mater.* **2016**, *16*, 363.
[15] D. Baran, T. Kirchartz, S. Wheeler, S. Dimitrov, M. Abdelsamie, J. Gorman, R. S. Ashraf, S. Holliday, A. Wadsworth, N. Gasparini, *Energy Environ. Sci.* **2016**, *9*, 3783.
[16] C. L. Cutting, M. Bag, D. Venkataraman, *J. Mater. Chem. C* **2016**, *4*, 10367.
[17] F. C. Krebs, S. A. Gevorgyan, B. Gholamkhass, S. Holdcroft, C. Schlenker, M. E. Thompson, B. C. Thompson, D. Olson, D. S. Ginley, S. E. Shaheen, H. N. Alshareef, J. W. Murphy, W. J. Youngblood, N. C. Heston, J. R. Reynolds, S. J. Jia, D. Laird, S. M. Tuladhar, J. G. A. Dane, P. Atienzar, J. Nelson, J. M. Kroon, M. M. Wienk, R. A. J. Janssen, K. Tvingstedt, F. L. Zhang, M. Andersson, O. Inganas, M. Lira-Cantu, R. de Bettignies, S. Guillerez, T. Aernouts, D. Cheyns, L. Lutsen, B. Zimmermann, U. Wurfel, M. Niggemann, H. F. Schleiermacher, P. Liska, M. Gratzel, P. Lianos, E. A. Katz, W. Lohwasser, B. Jannon, *Sol. Energy Mater. Sol. Cells* **2009**, *93*, 1968.
[18] A. J. Moulé, K. Meerholz, *Adv. Funct. Mater.* **2009**, *19*, 3028.
[19] L. J. A. Koster, N. C. Greenham, C. Groves, *J. Appl. Phys.* **2009**, *105*, 094510 .
[20] A. J. Moulé, *Curr. Opin. Solid State Mater. Sci.* **2010**, *14*, 123.
[21] F. C. Krebs, *Org. Electron.* **2009**, *10*, 761.
[22] F. C. Krebs, *Sol. Energy Mater. Sol. Cells* **2009**, *93*, 465.
[23] C. N. Hoth, R. Steim, P. Schilinsky, S. A. Choulis, S. F. Tedde, O. Hayden, C. J. Brabec, *Org. Electron.* **2009**, *10*, 587.
[24] D. Vak, S.-S. Kim, J. Jo, S.-H. Oh, S.-I. Na, J. Kim, D.-Y. Kim, *Appl. Phys. Lett.* **2007**, *91*, 081102.
[25] R. Green, A. Morfa, A. J. Ferguson, N. Kopidakis, G. Rumbles, S. E. Shaheen, *Appl. Phys. Lett.* **2008**, *92*, 033301.
[26] F. Machui, L. Lucera, G. D. Spyropoulos, J. Cordero, A. S. Ali, P. Kubis, T. Ameri, M. M. Voigt, C. J. Brabec, *Sol. Energy Mater. Sol. Cells* **2014**, *128*, 441.
[27] M. Bolognesi, M. Prosa, M. Tessarolo, G. Donati, S. Toffanin, M. Muccini, M. Seri, *Sol. Energy Mater. Sol. Cells* **2016**, *155*, 436.
[28] Y. R. Hong, P. K. Chen, J. C. Wang, M. K. Lee, S. F. Horng, H. F. Meng, *Sol. Energy Mater. Sol. Cells* **2014**, *120*, 197.
[29] S. L. Lim, E. C. Chen, C. Y. Chen, K. H. Ong, Z. K. Chen, H. F. Meng, *Sol. Energy Mater. Sol. Cells* **2012**, *107*, 292.
[30] A. Schneider, N. Traut, M. Hamburger, *Sol. Energy Mater. Sol. Cells* **2014**, *126*, 149.
[31] N. Shin, L. J. Richter, A. A. Herzing, R. J. Kline, D. M. DeLongchamp, *Adv. Energy Mater.* **2013**, *3*, 938.
[32] J. G. Tait, T. Merckx, W. Q. Li, C. Wong, R. Gehlhaar, D. Cheyns, M. Turbiez, P. Heremans, *Adv. Funct. Mater.* **2015**, *25*, 3393.
[33] P. T. Tsai, K. C. Yu, C. J. Chang, S. F. Horng, H. F. Meng, *Org. Electron.* **2015**, *22*, 166.
[34] W. Chen, M. P. Nikiforov, S. B. Darling, *Energy Environ. Sci.* **2012**, *5*, 8045.
[35] Y. Huang, E. J. Kramer, A. J. Heeger, G. C. Bazan, *Chem. Rev.* **2014**, *114*, 7006.
[36] D. M. DeLongchamp, R. J. Kline, A. Herzing, *Energy Environ. Sci.* **2012**, *5*, 5980.
[37] M. R. Hammond, R. J. Kline, A. A. Herzing, L. J. Richter, D. S. Germack, H. W. Ro, C. L. Soles, D. A. Fischer, T. Xu, L. P. Yu, M. F. Toney, D. M. DeLongchamp, *ACS Nano* **2011**, *5*, 8248.
[38] S. Barrau, V. Andersson, F. L. Zhang, S. Masich, J. Bijleveld, M. R. Andersson, O. Inganas, *Macromolecules* **2009**, *42*, 4646.
[39] J. Jo, S. I. Na, S. S. Kim, T. W. Lee, Y. Chung, S. J. Kang, D. Vak, D. Y. Kim, *Adv. Funct. Mater.* **2009**, *19*, 2398.
[40] S. D. Oosterhout, M. M. Wienk, S. S. van Bavel, R. Thiedmann, L. J. A. Koster, J. Gilot, J. Loos, V. Schmidt, R. A. J. Janssen, *Nat. Mater.* **2009**, *8*, 818.
[41] S. van Bavel, E. Sourty, G. de With, K. Frolic, J. Loos, *Macromolecules* **2009**, *42*, 7396.
[42] S. Vajjala Kesava, R. Dhanker, D. R. Kozub, K. Vakhshouri, U. H. Choi, R. H. Colby, C. Wang, A. Hexemer, N. C. Giebink, E. D. Gomez, *Chem. Mater.* **2013**, *25*, 2812.
[43] A. A. Herzing, L. J. Richter, I. M. Anderson, *J. Phys. Chem. C* **2010**, *114*, 17501.
[44] S. A. Hawks, J. C. Aguirre, L. T. Schelhas, R. J. Thompson, R. C. Huber, A. S. Ferreira, G. Zhang, A. A. Herzing, S. H. Tolbert, B. J. Schwartz, *J. Phys. Chem. C* **2014**, *118*, 17413.
[45] R. B. Ross, C. M. Cardona, D. M. Guldi, S. G. Sankaranarayanan, M. O. Reese, N. Kopidakis, J. Peet, B. Walker, G. C. Bazan, E. Van Keuren, B. C. Holloway, M. Drees, *Nat. Mater.* **2009**, *8*, 208.
[46] R. B. Ross, C. M. Cardona, F. B. Swain, D. M. Guldi, S. G. Sankaranarayanan, E. Van Keuren, B. C. Holloway, M. Drees, *Adv. Funct. Mater.* **2009**, *19*, 2332.
[47] J. D. Roehling, D. Baran, J. Sit, T. Kassar, T. Ameri, T. Unruh, C. J. Brabec, A. J. Moule, *Sci. Rep.* **2016**, *6*, 30915.
[48] J. D. Roehling, K. J. Batenburg, F. B. Swain, A. J. Moule, I. Arslan, *Adv. Funct. Mater.* **2013**, *23*, 2115.
[49] B. Goris, T. Roelandts, K. Batenburg, H. H. Mezerji, S. Bals, *Ultramicroscopy* **2013**, *127*, 40.
[50] D. Chen, B. Goris, F. Bleichrodt, H. H. Mezerji, S. Bals, K. J. Batenburg, G. de With, H. Friedrich, *Ultramicroscopy* **2014**, *147*, 137.
[51] O. Wodo, J. D. Roehling, A. J. Moule, B. Ganapathysubramanian, *Energy Environ. Sci.* **2013**, *6*, 3060.
[52] J. D. Roehling, C. W. Rochester, H. W. Ro, P. Wang, J. Majewski, K. J. Batenburg, I. Arslan, D. M. Delongchamp, A. J. Moule, *J. Polym. Sci., Part B: Polym. Phys.* **2014**, *52*, 1291.
[53] D. S. Germack, C. K. Chan, B. H. Hamadani, L. J. Richter, D. A. Fischer, D. J. Gundlach, D. M. DeLongchamp, *Appl. Phys. Lett.* **2009**, *94*, 155.
[54] D. S. Germack, C. K. Chan, R. J. Kline, D. A. Fischer, D. J. Gundlach, M. F. Toney, L. J. Richter, D. M. DeLongchamp, *Macromolecules* **2010**, *43*, 3828.
[55] X. N. Yang, J. Loos, S. C. Veenstra, W. J. H. Verhees, M. M. Wienk, J. M. Kroon, M. A. J. Michels, R. A. J. Janssen, *Nano Lett.* **2005**, *5*, 579.
[56] W. Ma, C. Yang, X. Gong, K. Lee, A. J. Heeger, *Adv. Funct. Mater.* **2005**, *15*, 1617.
[57] J. D. A. Lin, O. V. Mikhnenko, J. Chen, Z. Masri, A. Ruseckas, A. Mikhailovsky, R. P. Raab, J. Liu, P. W. M. Blom, M. A. Loi,

C. J. Garcia-Cervera, I. D. W. Samuel, T.-Q. Nguyen, *Mater. Horiz.* **2014**, *1*, 280.
[58] O. V. Mikhnenko, P. W. M. Blom, T.-Q. Nguyen, *Energy Environ. Sci.* **2015**, *8*, 1867.
[59] J. Nakamura, K. Murata, K. Takahashi, *Appl. Phys. Lett.* **2005**, *87*, 132105.
[60] G. Li, V. Shrotriya, J. Huang, Y. Yao, T. Moriarty, K. Emery, Y. Yang, *Nat. Mater.* **2005**, *4*, 864.
[61] A. J. Moule, D. Neher, S. T. Turner, in *P3HT Revisited—from Molecular Scale to Solar Cell Devices* (Ed: S. Ludwigs), Springer-Verlag Berlin Heidelberg, Berlin, Heidelberg, **2014**.
[62] B. Schmidt-Hansberg, M. F. G. Klein, K. Peters, F. Buss, J. Pfeifer, S. Walheim, A. Colsmann, U. Lemmer, P. Scharfer, W. Schabel, *J. Appl. Phys.* **2009**, *106*, 124501.
[63] P. W. M. Blom, V. D. Mihailetchi, L. J. A. Koster, D. E. Markov, *Adv. Mater.* **2007**, *19*, 1551.
[64] A. J. Moulé, J. B. Bonekamp, K. Meerholz, *J. Appl. Phys.* **2006**, *100*, 094503.
[65] J. Peet, J. Y. Kim, N. E. Coates, W. L. Ma, D. Moses, A. J. Heeger, G. C. Bazan, *Nat. Mater.* **2007**, *6*, 497.
[66] A. J. Moulé, K. Meerholz, *Adv. Mater.* **2008**, *20*, 240.
[67] M. Al-Ibrahim, O. Ambacher, S. Sensfuss, G. Gobsch, *Appl. Phys. Lett.* **2005**, *86*, 201120.
[68] F. Machui, S. Abbott, D. Waller, M. Koppe, C. J. Brabec, *Macromol. Chem. Phys.* **2011**, *212*, 2159.
[69] J. R. Kremer, D. N. Mastronarde, J. R. McIntosh, *J. Struct. Biol.* **1996**, *116*, 71.
[70] K. J. Batenburg, J. Sijbers, *IEEE Trans. Electron Devices* **2011**, *20*, 2542.
[71] W. van Aarle, W. J. Palenstijn, J. De Beenhouwer, T. Altantzis, S. Bals, K. J. Batenburg, J. Sijbers, *Ultramicroscopy* **2015**, *157*, 35.
[72] O. Wodo, S. Tirthapura, S. Chaudhary, B. Ganapathysubramanian, *Org. Electron.* **2012**, *13*, 1105.
[73] O. Wodo, S. Tirthapura, S. Chaudhary, B. Ganapathysubramanian, *J. Appl. Phys.* **2012**, *112*, 064316.
[74] P. Peumans, A. Yakimov, S. R. Forrest, *J. Appl. Phys.* **2003**, *93*, 3693.
[75] B. S. S. Pokuri, B. Ganapathysubramanian, *Modell. Simul. Mater. Sci. Eng.* **2016**, *24*, 065012.